

Crystallization and vitrification of electrons in a glass-forming charge liquid

S. Sasaki^{1,*}, K. Hashimoto^{1,*†}, R. Kobayashi¹, K. Itoh¹, S. Iguchi¹, Y. Nishio², Y. Ikemoto³, T. Moriwaki³, N. Yoneyama⁴, M. Watanabe⁵, A. Ueda⁶, H. Mori⁶, K. Kobayashi⁷, R. Kumai⁷, Y. Murakami⁷, J. Müller⁸, and T. Sasaki¹

¹*Institute for Materials Research, Tohoku University, Aoba-ku, Sendai 980-8577, Japan*

²*Department of Physics, Faculty of Science, Toho University, Funabashi, Chiba 274-8510, Japan*

³*SPring-8, Japan Synchrotron Radiation Research Institute, Sayo, Hyogo 679-5198, Japan*

⁴*Graduate Faculty of Interdisciplinary Research, University of Yamanashi, Kohu, Yamanashi 400-8511, Japan*

⁵*Institute of Multidisciplinary Research for Advanced Materials, Tohoku University, Sendai 980-8577, Japan*

⁶*The Institute for Solid State Physics, The University of Tokyo, Kashiwa, Chiba 277-8581, Japan*

⁷*CMRC and Photon Factory, Institute of Materials Structure Science,*

High Energy Accelerator Research Organization (KEK), Tsukuba, Ibaraki 305-0801, Japan

⁸*Institute of Physics, Goethe-University Frankfurt, Max-von-Laue-Str. 1, 60438 Frankfurt(M), Germany*

**These authors contributed equally to this work.*

[†]To whom correspondence should be addressed. E-mail: hashimoto@imr.tohoku.ac.jp (K.H.)

Charge ordering (CO) is a phenomenon in which electrons in solids crystallize into a periodic pattern of charge-rich and charge-poor sites owing to strong electron correlations, mostly resulting in long-range order. Recently, however, in geometrically-frustrated systems, a glassy electronic state without long-range CO has been observed. Here we report that a charge-ordered organic material with an isosceles triangular lattice shows non-equilibrium charge dynamics associated with crystallization and vitrification of electrons. We show that charge crystallization can be avoided by rapid cooling, and charge vitrification occurs through a supercooled charge-liquid state, accompanied by heterogeneous slow dynamics, which can be understood by an energy landscape with multiple local minima. We also reveal that the crystallization of electrons shares the same nucleation and growth processes as that of conventional glass-forming liquids. These surprising similarities among different classes of glass formers may provide new insights into our general understanding of the liquid–glass transition.

The physics of glassy materials is one of the deepest and most fascinating problems in solid state theory that remains unresolved [1]. Although significant progress has been made over the past several decades to better understand the dynamical aspects of the glass transition, the processes by which liquids acquire the glassy state upon cooling are not fully understood [2]. The most fundamental non-equilibrium dynamic phenomena associated with the liquid–glass transition process are crystallization and vitrification (Fig. 1a). These phenomena are competing and mutually exclusive, but closely related with each other [3, 4]. In glass-forming liquids, crystallization below the melting point T_m can be avoided when the system is cooled fast enough, leading to a supercooled liquid state accompanied by an increase in viscosity (Fig. 1a) [2, 5]. Upon further cooling, owing to the viscous retardation of crystallization, the supercooled liquid state freezes into a glassy state, that is, vitrification occurs at the glass-transition temperature T_g . Thus, the relationship between crystallization and vitrification is key to the understanding of the liquid–glass transition. Here, we demonstrate that this general picture can be extended to crystallization and vitrification of strongly correlated electrons re-

alized in a geometrically frustrated charge-ordered organic system θ_m -(BEDT-TTF)₂TlZn(SCN)₄, where BEDT-TTF denotes bis(ethylenedithio)tetrathiafulvalene. Surprising similarities between our system and conventional glass formers are observed in the crystallization and vitrification processes, which highlight the universal nature of the liquid–glass transition.

The quasi-two-dimensional (quasi-2D) organic materials θ -(BEDT-TTF)₂X consist of an alternating stack of a conducting BEDT-TTF layer with a triangular lattice and an insulating anion X layer [6, 7]. The charge transfer between these two layers leads to a 2D quarter-filled hole band system (that is, one hole per two BEDT-TTF molecules), in which the inter-site Coulomb repulsions give rise to an instability towards charge ordering (CO) [8]. Indeed, θ -(BEDT-TTF)₂RbZn(SCN)₄ (denoted as θ -RbZn) undergoes a CO transition at 190 K [6, 9], where the charge carriers are localized periodically with a horizontal stripe pattern. Such a periodic CO state can be regarded as a “charge-crystal” state [9]. In contrast, above the CO transition temperature, the charge of +0.5 per one BEDT-TTF molecule is distributed uniformly in space; therefore, such a delocalized state can be referred to as a “charge-liquid” state. Importantly, in θ -RbZn, when the sample is cooled faster than a critical cooling rate (~ 5 K/min), charge crystallization is kinetically avoided, leading to a “charge-glass” state where the charge is randomly quenched. In θ -(BEDT-TTF)₂CsZn(SCN)₄ (θ -CsZn) with a more isotropic triangular lattice, the critical cooling rate becomes much slower (Supplementary Information Sec. II). As a result, the charge-liquid state inevitably results in a charge-glass state even upon very slow cooling (< 0.1 K/min) [10]. The origin of the glassy electronic state, which therefore has been discussed experimentally [9–12] and theoretically [13] in terms of the geometrically frustrated triangular lattice, however, still remains rather elusive.

The system θ -(BEDT-TTF)₂TlZn(SCN)₄, which exists in two different crystal forms with orthorhombic and monoclinic symmetries (Supplementary Information Sec. II), may play a key role in the understanding of the charge-glass state. Orthorhombic θ_o -(BEDT-TTF)₂TlZn(SCN)₄ (θ_o -TlZn) exhibits a horizontal CO transition at 240 K, which is classified into the same category as θ -RbZn and θ -CsZn with orthorhom-

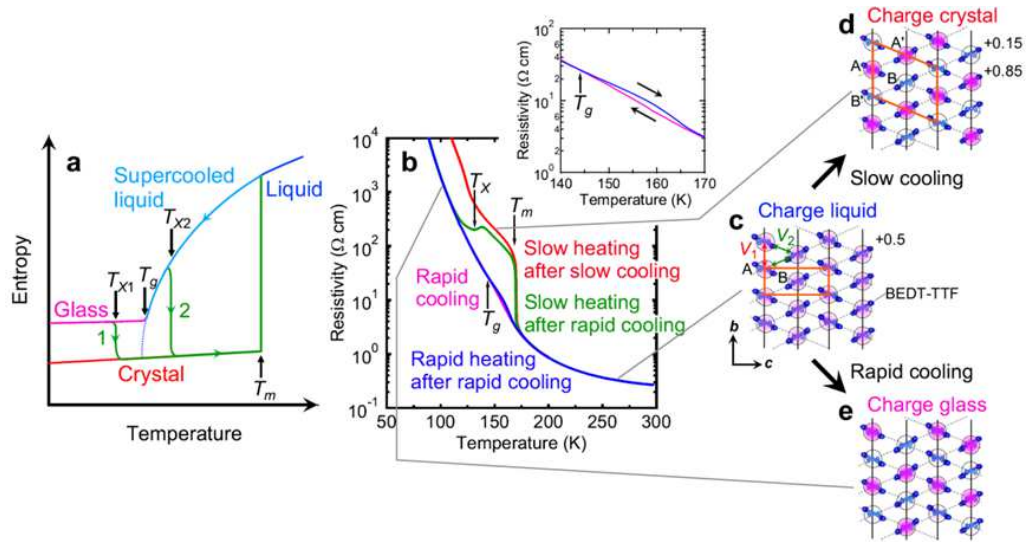


FIG. 1. (a) Generic entropy-temperature diagram of a glass-forming liquid. T_m is the melting temperature, T_g is the glass-transition temperature, and T_X is the crystallization temperature. A supercooled liquid state emerges when the liquid is cooled fast enough to avoid crystallization. A slower (faster) heating-rate process 1 (2) leads to a lower (higher) crystallization temperature T_{X1} (T_{X2}). (b) Temperature dependence of the resistivity for θ_m -TlZn measured in the rapid or slow heating process after rapid or slow cooling as well as in the rapid cooling process. One can see that charge crystallization occurs at T_X lower than T_g in the slow heating process after rapid cooling. The inset shows the hysteresis loop of the resistivity during the heating/cooling process at a sweeping rate of 100 K/min. (c–e) Schematic illustrations of (c) the charge-liquid state, (d) the charge-crystal state, and (e) the charge-glass state in θ_m -TlZn. The orange rectangles in (c) and (d) denote the unit cell. V_1 and V_2 are the nearest-neighbor Coulomb interactions, where $V_2/V_1 \sim 0.8$ (also see Fig. S1c). The A and B sites in (c) are crystallographically equivalent due to the screw axis along the b axis. In the charge-crystal state (d), the diagonal CO pattern is formed, where the charge-rich (+0.85) sites, A and A', and the charge-poor (+0.15) sites, B and B', are not crystallographically equivalent. It should be noted that the difference in the charge density between A and A' (B and B') is too small to be detected experimentally [16].

bic symmetry. Since the anisotropy of the triangular lattice is far from unity, the critical cooling rate for glass formation remains quite high [11, 12]. By contrast, the monoclinic θ_m -(BEDT-TTF) $_2$ TlZn(SCN) $_4$ (θ_m -TlZn) shows a diagonal CO transition at $T_m = 170$ K (Figs. 1b–d). The temperature-dependent resistivity $\rho(T)$ shows a strong sweeping-rate dependence below T_m (Fig. 1b), although the triangular lattice for θ_m -TlZn is more anisotropic than that for θ_o -TlZn. In θ_m -TlZn, the long-range CO transition can be avoided by rapid cooling (≥ 50 K/min), and charge vitrification occurs through a supercooled charge-liquid state (Figs. 1b and e). In the cooling/heating cycle of the ρ - T profile, a clear hysteresis loop associated with the glass transition is observed at 145–165 K (see the inset of Fig. 1b), which is very similar to what is observed in θ -CsZn [10]. We tentatively define the glass-transition temperature T_g as the temperature above which the resistivity starts to branch off.

In order to clarify the origin of charge-glass formation in θ_m -TlZn, we performed resistance noise measurements which are a powerful probe to detect slow dynamics associated with charge vitrification [9, 10]. Figure 2a shows a typical normalized noise power spectral density of the resistance fluctuations S_R/R^2 . The baseline of S_R/R^2 fits well to generic $1/f$ with a slightly deviating frequency exponent yielding $1/f^\alpha$ with $\alpha \sim 0.8$ – 0.9 . For clarity, $f^\alpha \times S_R/R^2$ is plotted in Fig. 2b, which clearly shows that the resistance fluctuations exhibit a broad peak structure. The data are well fit-

ted to the distributed Lorentzian model [9, 10] with a characteristic center frequency $f_c (= \sqrt{f_{c1}f_{c2}}$, where f_{c1} and f_{c2} are the high- and low-cutoff frequencies, respectively), from which we derived the temperature evolution of the relaxation time $\tau_c = 1/(2\pi f_c)$. Remarkably, the peak structure in $f^\alpha \times S_R/R^2$ becomes broader and more asymmetric with decreasing temperature (Figs. 2b and c), showing that the dynamics becomes more heterogeneous. In addition, as shown in Fig. 2d, τ_c exhibits a drastic slowing down over several orders of magnitude, and seems to reach to 10^2 – 10^3 seconds around $T_g \sim 145$ K, if we assume that τ_c obeys the Arrhenius law as observed in θ -CsZn [10] and as expected in recent Monte Carlo simulations [13]. These results indicate the emergence of slow dynamics accompanied by dynamic heterogeneity towards the charge-glass transition.

Clarifying the relationship between the heterogeneous slow dynamics and local charge configurations may be key to the understanding of charge-glass formation [3, 14]. To this end, we investigated charge disproportionation at a microscopic level by means of a charge-sensitive vibrational mode ν_{27} of the BEDT-TTF molecule. The ν_{27} mode is known as a local probe of the molecular charge ρ_c [15], and splits into two modes ν_{27I} and ν_{27N} in the presence of charge disproportionation between the A and B sites in the unit cell (see Fig. 1c and Fig. 2e), where the subscripts I and N represent the hole-rich and hole-poor sites, respectively. Figure 2f shows the temperature dependence of the polarized optical conductiv-

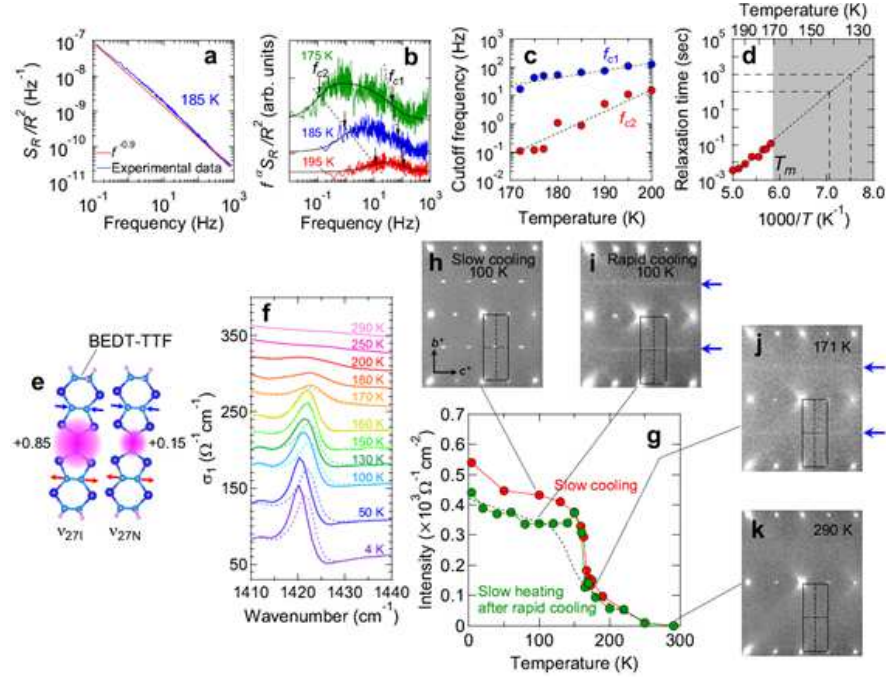


FIG. 2. (a) Typical normalized resistance noise power spectral density at 185 K. The red line indicates a fit to a background $S_R/R^2 \propto 1/f^\alpha$ with $\alpha = 0.9$. (b) Power spectral density multiplied by f^α at various temperatures above T_m . The black solid curves represent fits to the distributed Lorentzian model [9, 10] with a characteristic center frequency $f_c = \sqrt{f_{c1}f_{c2}}$, where f_{c1} and f_{c2} are the high- and low-frequency cutoffs, respectively. The dotted lines are guides for the eyes. (c) Temperature dependence of the cutoff frequencies f_{c1} and f_{c2} . The dotted lines are eye guides. (d) Arrhenius plot of the relaxation time $\tau_c = 1/(2\pi f_c)$ derived from the power spectral density. The dotted line is a fit to the Arrhenius law, $\tau_0 \exp(\frac{\Delta}{k_B T})$ with $\tau_0 = 10^{-14}$ sec and $\Delta/k_B = 5200$ K. The gap value corresponds to the energy scale of barriers in an energy landscape as illustrated in Fig. 3b. The charge crystallization process prevents measurements in the supercooled charge-liquid state (gray hatched area). (e) Sketch of the infrared active vibrational mode ν_{27} of the BEDT-TTF molecule. The center frequency is represented by $\nu_{27}(\rho_c) = 1398 \text{ cm}^{-1} + 140(1 - \rho_c) \text{ cm}^{-1}$ [15]. The charge-rich (ν_{27I}) and charge-poor (ν_{27N}) sites are observed at 1420 cm^{-1} and 1515 cm^{-1} , respectively (Supplementary Information Sec. IV). (f) Temperature dependence of $\sigma_1(\omega)$ for the polarization of $\mathbf{E} \parallel \mathbf{c}$ measured during slow cooling (solid line) and slow heating after rapid cooling (dashed line). (g) Temperature dependence of the ν_{27I} mode intensity. The dotted curve is an eye guide. An upturn observed above ~ 120 K during slow heating after rapid cooling is attributed to charge crystallization. (h), (i) Oscillation photographs of the b^*-c^* plane measured at 100 K after (h) slow and (i) rapid cooling. In the charge-crystal state (h), clear satellite peaks appear at $\mathbf{q}_0 = (1/2 \ 1/2)$. By contrast, in the charge-glass state (i), diffuse lines of $\mathbf{q}_d = (1/2 \ l)$ are observed. (j), (k) Oscillation photographs of the b^*-c^* plane measured at (j) 171 K and (k) 290 K. At room temperature, only Bragg reflections exist. In contrast, diffuse lines at $\mathbf{q}_d = (1/2 \ l)$ are observed above T_m . The blue arrows in (i) and (j) indicate the diffuse lines.

ity spectra. A clear peak around 1420 cm^{-1} is assigned to the ν_{27I} mode ($\rho_c \sim 0.85$) [16]. Importantly, a sizable intensity of ν_{27I} has been observed above T_m (Fig. 2g), indicating the presence of charge disproportionation above T_m . Here, it should be noted that since the A and B sites are crystallographically equivalent above T_m due to the screw axis along the b axis [16], the time-averaged charge distribution above T_m is $+0.5$ per one BEDT-TTF molecule (Fig. 1c). Therefore, the splitting of ν_{27} above T_m implies that charge disproportionation above T_m is not static, but dynamically fluctuating in the timescale slower than the molecular vibrational ν_{27} motion. Since the intensity of ν_{27I} is considered to reflect the volume of dynamically fluctuating charge clusters, its increase with decreasing temperature suggests that the heterogeneous slow dynamics observed in the noise measurements are caused by the dynamically fluctuating charge clusters.

To obtain insights into the structural origin of the heterogeneous slow dynamics, we performed X-ray diffuse scatter-

ing measurements. Oscillation photographs measured at various temperatures are shown in Figs. 2h–k. At room temperature, only Bragg reflections are observed (Fig. 2k), whereas in the charge-crystal state clear satellite peaks appear at $\mathbf{q}_0 = (1/2 \ 1/2)$, compatible with the diagonal CO pattern (Fig. 2h). Theoretical calculations for the θ -type materials based on the extended Hubbard model (EHM) [17] have suggested that the diagonal CO pattern is most stable when $V_1 > V_2$, which is consistent with the observations in the charge-crystal state of θ_m -TlZn. In contrast, in the charge-glass state, diffuse lines at $\mathbf{q}_d = (1/2 \ l)$ are observed (Fig. 2i). The origin of the diffuse lines may be ascribed to geometric frustration. The classical ground states of the t - V model, which is the spinless version of the EHM, on an isosceles triangular lattice are known to be disordered owing to geometric frustration when $V_1 \geq V_2$ [18, 19] (also see Supplementary Information Sec. III). At $V_1 = V_2$, the ground state has a “macroscopic” disordered ground state with a degeneracy of $\sim 2^{N-1}$ (N is the number

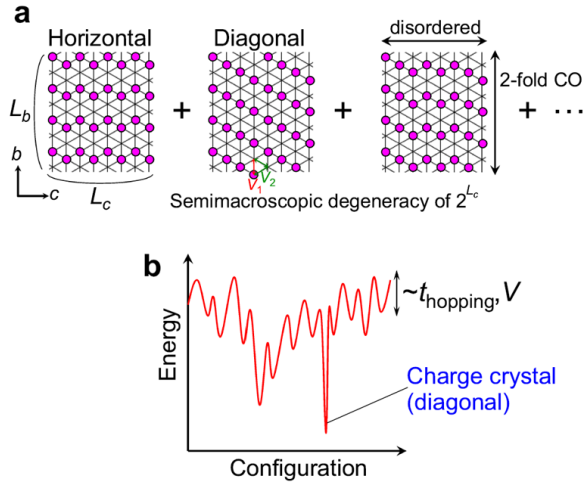


FIG. 3. (a) Schematics of chain striped CO patterns such as horizontal, diagonal, and so on. The magenta circles represent the charge-rich sites. V_1 and V_2 ($V_1 > V_2$) are the nearest-neighbor Coulomb interactions. Since all these states are degenerate in the classical limit of the t - V model, the classical ground state can be described by the superposition of these states, which has a degeneracy of 2^{L_c} , where L_c is the system length in the c direction. The number of lattice sites N is given by $L_b \times L_c$. (b) Schematic illustration of an energy landscape with multiple local minima separated by barriers having an energy scale of the hopping integral t_{hopping} and/or the long-range Coulomb interaction V (~ 1 eV).

of lattice sites). On the other hand, at $V_1 > V_2$, V_1 preferentially determines the two-fold periodic striped CO pattern along the b direction, whereas the geometric frustration between the two diagonal V_2 gives rise to a “semimacroscopic” degeneracy of 2^{L_c} , where L_c is the system length in the c direction (Fig. 3a). What is important here is that an introduction of a small quantum hopping term as well as a long-range Coulomb potential lifts the degeneracy, which drives the system to the diagonal CO pattern [13, 17]; however, the degeneracy remains in the wide temperature range above the ordering temperature [13]. This situation may induce an energy landscape with multiple local minima as illustrated in Fig. 3b, that is, a metastable state with an amorphous stripe-glass structure as proposed in Ref. 13, which in turn causes the heterogeneous slow dynamics in θ_m -TiZn. Although glassy states of electrons are often observed on the verge of the metal-insulator transition, these states are not caused by intrinsic properties of strongly correlated electrons, but rather by impurities or randomness [20]. The present results suggest that geometric frustration as well as strong quantum effects play an important role for the realization of quantum glasses essentially free from impurities or defects [21–23].

We now examine details of the charge crystallization process in order to clarify the relationship between crystallization and vitrification of electrons in θ_m -TiZn. Figure 4a displays the time evolution of the resistivity during the charge crystallization process from the supercooled charge-liquid or charge-glass state (Supplementary Information Sec. I). The magnitude of the resistivity, which is a measure of the crystallization

progress, increases with time, and then saturates. The relaxation time becomes faster with decreasing temperature, and then slower below 157 K, which is referred to as the “nose temperature”; this characteristic temperature dependence of the relaxation time can be explained by the theory of nucleation and growth at a first-order liquid-crystal phase transition (Supplementary Information Sec. VI).

In this study, in order to quantitatively evaluate the CO volume fraction from the resistivity, we used the effective medium percolation theory [24]. This theory describes a percolating current passing through an inhomogeneous mixture of conducting and insulating media (Supplementary Information Sec. V). By using a generalized effective medium (GEM) equation [25], we obtained the time evolution of the CO volume fraction, $\phi(t)$, at various temperatures (Figs. 4b and c). In the high-temperature region, $\phi(t)$ can be well fitted over the whole time range by the Johnson-Mehl-Avrami-Kolmogorov (JMAK) formula describing a conventional nucleation and growth process, $\propto 1 - \exp(-kt^n)$, where k and n are the JMAK parameters [26] (Fig. 4d, also see Supplementary Information Sec. VIII). By contrast, near the nose temperature, $\phi(t)$ can be fitted to the JMAK formula only in the early stage of crystal growth (Fig. 4e). For later time, a crossover to the Ostwald ripening that describes a rearrangement of crystal grain boundaries, $\propto 1 - (1 + k't)^{-1/3}$, where k' is a constant [27], explains the observed more moderate time evolution of $\phi(t)$. Such a process is often observed in the final stage of crystal growth (Supplementary Information Sec. VIII). Interestingly, below 145 K, $\phi(t)$ again exhibits a steep increase over the whole time range, which can be fitted to the JMAK formula (Fig. 4f). This temperature well coincides with T_g . Crystallization below T_g is studied in many fields of materials science, and an enhancement of the crystallization rate at T_g has been reported [28, 29]. The origin has been discussed, for example, in terms of a crystal-glass interface [28, 29]. In this scenario, the volume contraction upon crystallization below T_g provides free volume for atoms or molecules surrounding the crystal, which leads to a mobility increase at the crystal-glass interface, resulting in an enhancement of the crystal growth rate at T_g . We speculate that the same surface dynamics occurs at the charge-crystal/glass interface in θ_m -TiZn.

Figure 4g displays the contour map of the CO fraction plotted in the time-temperature plane, that is, the so-called time-temperature-transformation (TTT) diagram. The obtained TTT diagram clearly reflects the two characteristic features discussed above; one is the nose structure around 160 K, and the other is the enhancement of crystal growth at T_g . These observations demonstrate that the crystallization process of electrons in solids can be described by the nucleation and growth process of a liquid, as observed in conventional glass-forming liquids such as structural and metallic glasses [28–31], and charge crystallization and vitrification are closely related with each other. These findings of the dynamical properties in the glass-forming charge liquid highlight the universal nature of the dynamic processes observed in quite different varieties of glass-forming systems and may provide insights towards a general understanding of the liquid-glass transition.

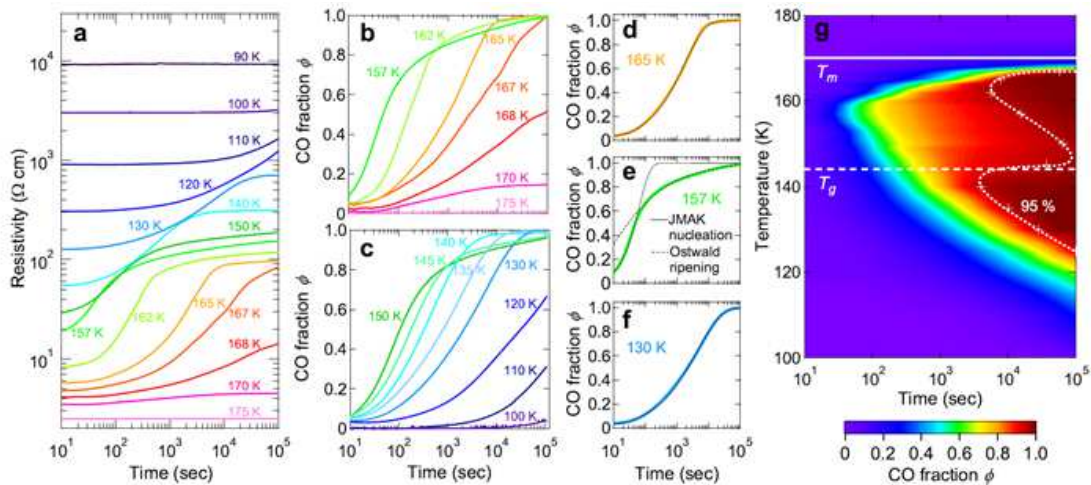


FIG. 4. (a) Time-dependent resistivity change during the charge crystallization process measured at various temperatures. (b), (c) Time evolution of the CO volume fraction $\phi(t)$ calculated from the effective medium percolation theory (b) above and (c) below the nose temperature. (d)–(f) $\phi(t)$ at (d) 165 K, (e) 157 K, and (f) 130 K along with fits by the JMAK formula (solid curve), $\phi(t) = 1 - \exp(-kt^n)$, where k and n are the JMAK parameters, and the Ostwald ripening process (dotted curve), $\phi(t) = 1 - (1 + k't)^{-1/3}$, where k' is a constant. (g) TTT diagram derived from $\phi(t)$ in (b) and (c). The dotted curve is an eye guide connecting the data points where $\phi(t) = 0.95$.

ACKNOWLEDGMENTS

We thank K. Yoshimi, T. Kato, M. Naka, H. Shiba, and C. Hotta for fruitful discussion. We also thank J. Kudo and M. Kurosu for technical assistance. Synchrotron radiation measurements were performed at SPring-8 with the approvals of JASRI (2014B1340, 2014B1752, 2015A1777, 2015B1752, and 2016A0073). X-ray diffraction study was performed under the approval of the Photon Factory Program Advisory

Committee (Proposal No.2014S2-001). This work was supported by a Grant-in-Aid for Scientific Research (Grants No. 24340074, No. 25287080, No. 26610096, No. 26102014, No. 15H00984, No. 15H00988, No. 15K13511, No. 15K17688, No. 16H04010, No. 16K05430, and No. 16K05744) from MEXT and JSPS, by a Grant-in-Aid for Scientific Research on Innovative Areas “ π -Figuration” (No. 26102001), and by the Canon Foundation.

- [1] P.W. Anderson, Through a glass lightly. *Science* **267**, 1615 (1995).
- [2] P. G. Debenedetti, F. H. Stillinger, Supercooled liquids and the glass transition. *Nature* **410**, 259–267 (2001).
- [3] H. Shintani, H. Tanaka, Frustration on the way to crystallization in glass. *Nature Phys.* **2**, 200–206 (2006).
- [4] T. Kawasaki, H. Tanaka, Formation of a crystal nucleus from liquid. *Proc. Natl. Acad. Sci. USA* **107**, 14036–14041 (2010).
- [5] C. A. Angell, Perspective on the glass transition. *J. Phys. Chem. Solids* **49**, 863–871 (1988).
- [6] H. Mori, S. Tanaka, T. Mori, Systematic study of the electronic state in θ -type BEDT-TTF organic conductors by changing the electronic correlation. *Phys. Rev. B* **57**, 12023–12029 (1998).
- [7] F. Sawano *et al.*, An organic thyristor. *Nature* **437**, 522 (2005).
- [8] H. Seo, Charge ordering in organic ET compounds. *J. Phys. Soc. Jpn* **69**, 805–820 (2000).
- [9] F. Kagawa *et al.*, Charge-cluster glass in an organic conductor. *Nature Phys.* **9**, 419–422 (2013).
- [10] T. Sato *et al.*, Emergence of nonequilibrium charge dynamics in a charge-cluster glass. *Phys. Rev. B* **89**, 121102(R) (2014).
- [11] T. Sato *et al.*, Systematic variations in the charge-glass-forming ability of geometrically frustrated θ -(BEDT-TTF)₂X organic conductors. *J. Phys. Soc. Jpn* **83**, 083602 (2014).
- [12] H. Oike *et al.*, Phase-change memory function of correlated electrons in organic conductors. *Phys. Rev. B* **91**, 041101(R) (2015).
- [13] S. Mahmoudian *et al.*, Glassy dynamics in geometrically frustrated Coulomb liquids without disorder. *Phys. Rev. Lett.* **115**, 025701 (2015).
- [14] M. D. Ediger, P. Harrowell, Perspective: Supercooled liquids and glasses. *J. Chem. Phys.* **137**, 080901 (2012).
- [15] T. Yamamoto *et al.*, Examination of the charge-sensitive vibrational modes in bis(ethylenedithio)tetrathiafulvalene. *J. Phys. Chem B* **109**, 15226–15235 (2005).
- [16] K. Suzuki, K. Yamamoto, K. Yakushi, Charge-ordering transition in orthorhombic and monoclinic single-crystals of θ -(BEDT-TTF)₂TlZn(SCN)₄ studied by vibrational spectroscopy. *Phys. Rev. B* **69**, 085114 (2004).
- [17] M. Naka, H. Seo, Long-period charge correlations in charge-frustrated molecular θ -(BEDT-TTF)₂X. *J. Phys. Soc. Jpn* **83**, 053706 (2014).
- [18] C. Hotta, N. Furukawa, Strong coupling theory of the spinless charges on triangular lattices: Possible formation of a gapless charge-ordered liquid. *Phys. Rev. B* **74**, 193107 (2006).
- [19] Y. Han *et al.*, Geometric frustration in buckled colloidal monolayers. *Nature* **456**, 898–903 (2008).

- [20] E. Dagotto, Complexity in strongly correlated electronic systems. *Science* **309**, 257–262 (2005).
- [21] J. Schmalian, P.G. Wolyes, Stripe glasses: Self-generated randomness in a uniformly frustrated system. *Phys. Rev. Lett.* **85**, 836–839 (2000).
- [22] R. Jamei, S. Kivelson, B. Spivak, Universal aspects of Coulomb-frustrated phase separation. *Phys. Rev. Lett.* **94**, 056805 (2005).
- [23] K. Yoshimi, H. Maebashi, Coulomb frustrated phase separation in quasi-two-dimensional organic conductors on the verge of charge ordering. *J. Phys. Soc. Jpn* **81**, 063003 (2012).
- [24] D. Stauffer, A. Aharony, *Introduction to Percolation Theory*. Taylor and Francis, London, second edition, (1994).
- [25] D.S. McLachlan, M. Blazkiewicz, R. E. Newnham, Electrical resistivity of composites. *J. Am. Ceram. Soc.* **73**, 2187–2203 (1990).
- [26] M. Avrami, Kinetics of phase change. I General theory. *J. Chem. Phys.* **7**, 1103 (1939).
- [27] I. M. Lifshitz, V. V. Slyozov, The kinetics of precipitation from supersaturated solid solutions. *J. Phys. Chem. Solids.* **19**, 35–50 (1961).
- [28] T. Konishi, H. Tanaka, Possible origin of enhanced crystal growth in a glass. *Phys. Rev. B* **76**, 220201(R) (2007).
- [29] Y. Sun, L. Zhu, K.L. Kearns, M.D. Ediger, L. Yu, Glasses crystallize rapidly at free surfaces by growing crystals upward. *Proc. Natl. Acad. Sci. USA* **108**, 5990–5995 (2011).
- [30] Y.J. Kim, R. Busch, W.L. Johnson, A.J. Rulison, W.K. Rhim, Experimental determination of a time–temperature–transformation diagram of the undercooled $Zr_{41.2}Ti_{13.8}Cu_{12.5}Ni_{10.0}Be_{22.5}$ alloy using the containerless electrostatic levitation processing technique. *Appl. Phys. Lett.* **68**, 1057–1059 (1996).
- [31] E. B. Moore, V. Molinero, Structural transformation in supercooled water controls the crystallization rate of ice. *Nature* **479**, 506–508 (2001).

Supplementary Information: Crystallization and vitrification of electrons in a glass-forming charge liquid

I. EXPERIMENTAL METHODS

Single crystals of the monoclinic θ_m -(BEDT-TTF)₂TiZn(SCN)₄ were grown by the electrochemical oxidation method. The typical size of the crystals used for the resistivity, noise spectroscopy, and optical conductivity measurements was $\sim 0.1 \text{ mm} \times 1 \text{ mm} \times 0.3 \text{ mm}$. For the X-ray diffraction measurements, smaller crystals ($\sim 0.03 \text{ mm} \times 0.3 \text{ mm} \times 0.1$) were selected. The resistivity measurements were carried out with a current flow along the b axis. The electrical contacts were made using carbon paste. The TTT diagram was constructed from the time-dependent resistivity change during the charge crystallization process at the various temperatures. The experimental procedure is as follows; first, the sample was cooled rapidly ($>50 \text{ K/min}$) down to 50 K from the initial temperature of 200 K, and then heated up to each target temperature at a rate of 50 K/min, and finally held at the target temperature during each measurement. The noise measurements were performed by a standard five-probe method including a center ground terminal [S1]. Thereby, the sample forms a part of a Wheatstone bridge circuit in order to cancel out the constant voltage offset between the two voltage terminals. A sinusoidal current with an operating frequency of 997 Hz was applied along the b axis. The voltage signal was detected by a lock-in amplifier (SR830) and processed by a spectrum analyzer (Agilent 35670A). The experiment was carried out above $T_m = 170 \text{ K}$, since the charge crystallization process prevents measurements in the supercooled charge-liquid state. The polarized optical conductivity measurements were carried out with a Fourier transform microscope spectrometer in the range of 600–8000 cm^{-1} . A synchrotron radiation light source at BL43IR in SPring-8 was used. The optical conductivity was calculated through a Kramers-Kronig (KK) transformation from the optical reflectivity determined by comparison with a gold thin film evaporated on the sample surface. The X-ray diffraction measurements were performed by using a synchrotron radiation source ($\lambda = 1.0 \text{ \AA}$) at the Photon Factory (PF) BL-8A in the High Energy Accelerator Research Organization (KEK). The diffraction data were collected on an Imaging plate system (Rigaku). The oscillation angle of each photograph was 4 or 5°.

II. CRITICAL COOLING RATE FOR CHARGE-GLASS FORMATION

In θ -(BEDT-TTF)₂ MM' (SCN)₄ ($M = \text{Ti, Rb, Cs, } M' = \text{Zn, Co}$), there are two crystal forms with orthorhombic ($I222$) and monoclinic ($C2$) symmetries [S2]. Figure S1a and b shows the 2D molecular arrangement of the BEDT-TTF layer

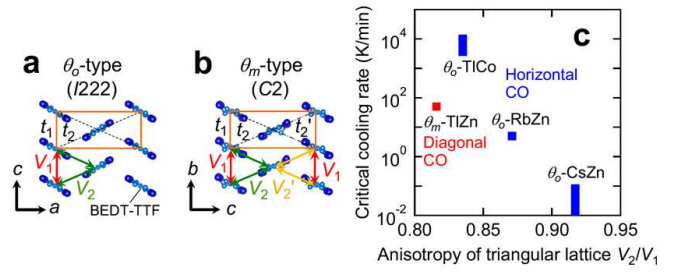


Fig. S1. (a), (b) 2D conducting BEDT-TTF layers within (a) the a - c plane for the θ_o -type salts and (b) the b - c plane for the θ_m -type salts. The orange rectangles indicate the unit cell. (c) Critical cooling rate for charge-glass formation as a function of V_2/V_1 for the various θ -type materials.

for the orthorhombic θ_o -type system and the monoclinic θ_m -type system, respectively. The intermolecular transfer integrals (the nearest-neighbor Coulomb interactions) are given by t_1 (V_1) and t_2 (V_2) in the θ_o -type system and by t_1 (V_1), t_2 (V_2), and t'_2 (V'_2) in the θ_m -type system. It should be noted that $t_2 \approx t'_2$ and $V_2 \approx V'_2$ for the θ_m -type system [S2, S3]. While the θ_o -type salts exhibit the horizontal CO transition, the θ_m -type salts show the diagonal CO transition [S4]. As discussed in Ref. S5, the material dependence of the critical cooling rate for charge-glass formation in the θ_o -type salts can be understood in terms of the anisotropy of the triangular lattice, V_2/V_1 (Fig. S1c). With decreasing V_2/V_1 (that is, with increasing the anisotropy of the triangular lattice), the critical cooling rate becomes fast, indicating that geometrical charge frustration between V_1 and V_2 plays an important role for the charge-glass formation in the θ_o -type salts. Here, we plot the critical cooling rate for θ_m -TiZn obtained in this study in Fig. S1c. In spite of the smaller value of V_2/V_1 , the critical cooling rate of θ_m -TiZn is slower than that of θ_o -TiCo, suggesting different mechanisms of charge-glass formation between these two systems, as discussed in the next section.

III. EXTENDED HUBBARD MODEL AND SPINLESS FERMION MODEL

The ground-state properties of θ -(BEDT-TTF)₂ X have been extensively studied by the extended Hubbard model (EHM) on an anisotropic triangular lattice [S3, S6–S12]. The Hamiltonian of the EHM is given by

$$\mathcal{H}_{\text{EHM}} = \sum_{\langle i,j \rangle \sigma} \left(-t_{ij} c_{i\sigma}^\dagger c_{j\sigma} + \text{h.c.} \right) + U \sum_i n_{i\uparrow} n_{i\downarrow} + \sum_{\langle i,j \rangle} V_{ij} n_i n_j, \quad (\text{S1})$$

where $c_{i\sigma}^\dagger$ ($c_{i\sigma}$) is the creation (annihilation) operator for a hole at the i -th site with spin σ (\uparrow or \downarrow), n_i ($\equiv \sum_\sigma n_{i\sigma}$) ($\equiv \sum_\sigma c_{i\sigma}^\dagger c_{i\sigma}$) is the number operator, t_{ij} and V_{ij} are the transfer integrals and the intersite Coulomb interactions between the i -th and j -th sites, respectively, and U is the on-site Coulomb repulsion. When $U \gg t_{ij}$, the EHM is compatible to the spinless fermion model (t - V model) that neglects the spin degrees

of freedom. The Hamiltonian of the t - V model is given by

$$\mathcal{H}_{t-V} = \sum_{\langle i,j \rangle} \left(-t_{ij} f_i^\dagger f_j + \text{h.c.} + V_{ij} \tilde{n}_i \tilde{n}_j \right), \quad (\text{S2})$$

where f_i^\dagger (f_i) is the creation (annihilation) operator for a spinless fermion at the i -th site and $\tilde{n}_i = f_i^\dagger f_i$ is the number operator. It has been well established that the classical ground states of the t - V model ($t_{ij} = 0$) on an isosceles triangle lattice as depicted in Fig. S2a are disordered owing to geometric frustration when $V_1 \geq V_2$, whereas the vertical CO becomes a unique ground state at $V_1 < V_2$ [S13–S16]. At $V_1 > V_2$, the chain-striped states such as the horizontal and diagonal COs emerge owing to the geometric frustration between the two diagonal Coulomb interactions V_2 , which is the case for θ_m -TlZn. When $V_1 = V_2$, the ground states include the vertical-striped state (Fig. S2a), the chain-striped states (Figs. S2b and c), and a three-sublattice state (Fig. S2d), all of which are degenerate. The last one has been discussed in terms of a “pin-ball liquid” [S15]. The orthorhombic θ_o -type compounds may be categorized in this regime. Indeed, three-fold diffuse rods have been observed in θ_o -RbZn [S17–S19] and θ_o -CsZn [S20–S22], which are different from what is observed in θ_m -TlZn. Thus, the anisotropy of V_2/V_1 is considered to play a crucial role for the different mechanisms of charge-glass formation in the θ -type materials (also see Fig. S1c).

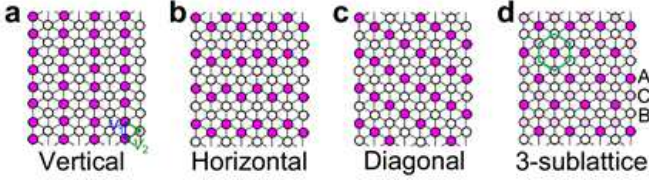


Fig. S2. Schematic charge configurations on the isosceles triangular lattice: (a) vertical CO, (b) horizontal CO, (c) diagonal CO, and (d) three-sublattice CO. The magenta and white circles represent the charge-rich and charge-poor sites, respectively. In the three-sublattice structure, the sublattice A is filled by one hole (“pin”), the sublattice B is empty, and the sublattice C is randomly occupied by the remaining holes (“ball”). The green hexagon in (d) stands for the unit cell.

IV. ASSIGNMENT OF VIBRATIONAL MODES IN OPTICAL CONDUCTIVITY

As shown in Fig. S3a, the BEDT-TTF molecule has three C=C stretching modes: two Raman-active modes $\nu_2(a_g)$ and $\nu_3(a_g)$, and one infrared-active mode $\nu_{27}(b_{1u})$. Figure S3b shows the optical conductivity spectra $\sigma_1(\omega)$ of θ_m -TlZn for the polarization of $\mathbf{E} \parallel \mathbf{c}$ in the charge-crystal state at 4 K and the charge-liquid state at 180 K. In the charge-crystal state, several vibrational modes of the BEDT-TTF molecule have been observed. According to Ref. S4, a few peaks around 1400 cm^{-1} can be ascribed to the CH_2 bending modes ν_{28} and ν_{45} , and broad bands at 1455 cm^{-1} and 1480 cm^{-1} can be assigned to ν_{3N} and ν_{2I} , respectively. It should be noted that

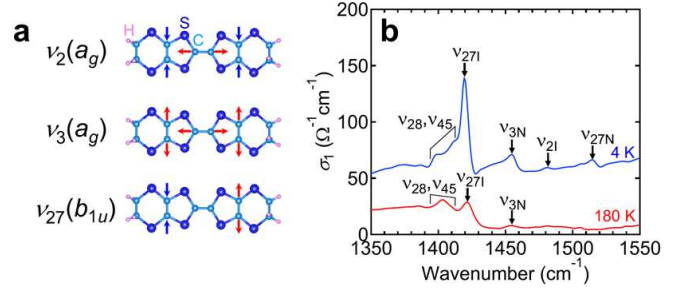


Fig. S3. (a) Schematic illustrations of three charge-sensitive C=C stretching modes of the BEDT-TTF molecule, $\nu_2(a_g)$, $\nu_3(a_g)$, and $\nu_{27}(b_{1u})$. The arrows indicate the shrinkage directions of the C=C bonds. (b) Polarized optical conductivity spectra ($\mathbf{E} \parallel \mathbf{c}$) of θ_m -TlZn in the charge-crystal state at 4 K and the charge-liquid state at 180 K. For clarity, $\sigma_1(\omega)$ at 180 K is offset. The subscripts I and N represent the hole-rich and hole-poor sites, respectively.

the Raman-active ν_2 and ν_3 modes become infrared-active because of weak dimerization of the two face-to-face BEDT-TTF molecules along the b direction. While the largest band at 1420 cm^{-1} corresponds to ν_{27I} , a small band at 1515 cm^{-1} is assigned to ν_{27N} . Usually, the ν_{27} mode is observed for the polarization along the long molecular axis of BEDT-TTF, namely, along the a axis in the case of θ_m -TlZn. However, the ν_{27} mode can be observed for the polarization along the c direction in θ_m -TlZn because the BEDT-TTF molecular long axis in θ_m -TlZn is tilted by 20° within the a - c plane [S4]. Some of the vibrational modes become smeared by thermal fluctuations with increasing temperature. Especially, the intensity of the ν_{27N} mode becomes too small to detect experimentally above ~ 100 K. Indeed, numerical calculations based on the vibronic adiabatic Mulliken theory [S23] predict that the intensity of the ν_{27N} band is about 3% of the ν_{27I} band when the charge disproportionation ratio is 0.85:0.15 [S4]. Therefore, in this study, we utilized the ν_{27I} mode to investigate the temperature evolution of charge disproportionation in θ_m -TlZn.

V. EFFECTIVE MEDIUM PERCOLATION THEORY

In this study, we used the generalized effective medium (GEM) equation [S24] to obtain the time evolution of the CO volume fraction $\phi(t)$ from the resistivity. A generalized effective medium (GEM) equation with two morphology parameters ϕ_0 and μ is given by [S24]

$$\frac{\phi(\sigma_l^{1/\mu} - \sigma_m^{1/\mu})}{\sigma_l^{1/\mu} + [\phi_0/(1 - \phi_0)]\sigma_m^{1/\mu}} + \frac{(1 - \phi)(\sigma_h^{1/\mu} - \sigma_m^{1/\mu})}{\sigma_h^{1/\mu} + [\phi_0/(1 - \phi_0)]\sigma_m^{1/\mu}} = 0, \quad (\text{S3})$$

where ϕ is the volume fraction of the insulating component (namely, in our case, the CO volume fraction) and ϕ_0 is the critical volume fraction at which the percolation path is closed by insulating CO domains. Here, σ_h (σ_l) is the conductivity of the metallic (insulating) component, σ_m is the conductivity of the medium itself, and μ is an exponent depending on

the dimensionality. While σ_l was measured in the slow heating process after slow cooling, σ_h was obtained in the rapid cooling process. The values of ϕ_0 and μ have been calculated by using numerical simulations for various 2D and 3D crystal lattices [S25, S26]. For the 2D triangular lattice, ϕ_0 and μ are estimated to be 0.66 (ref. S25) and 1.31 (ref. S26), respectively. By using these values, we obtained the time evolution of the CO volume fraction, $\phi(t)$, at the various temperatures (Figs. 4b and c).

VI. TIME-TEMPERATURE-TRANSFORMATION (TTT) DIAGRAM

The crystallization rate below the melting temperature T_m in the time-temperature-transformation (TTT) diagram can be described by the nucleation and growth process in a first-order phase transition of a liquid. Since the free energies of the crystal and liquid phases intersect at T_m , if crystallization is avoided by rapid cooling, a supercooled liquid state emerges, where the driving force for nucleation is caused by the difference in the free energy between crystal and liquid, $\Delta G = G_{\text{crystal}} - G_{\text{liquid}}$ (see Fig. S4a). In the supercooled liquid state, the crystallization rate is given by $I = \exp(-\frac{\Delta g(r=r^*)}{k_B T}) \times \exp(-\frac{G_m}{k_B T})$, where $\Delta g(r)$ is the change in the total Gibbs free energy caused by the nucleated crystalline phase, G_m is the activation energy for translational diffusion, r is the radius of the nucleus, r^* is a critical radius, and k_B is the Boltzmann's constant. The former is a thermodynamic term, and the latter is a kinetic term. $\Delta g(r)$ is given by $4\pi r^2 \sigma - (4/3)\pi r^3 \Delta G$ (where σ is the surface energy), which has a thermodynamic energy barrier of $(16/3)\pi \sigma^3 / (\Delta G)^2$ at the critical radius $r^* = 2\sigma / \Delta G$ (see Fig. S4b). For nucleation, the nucleus is needed to overcome the thermodynamic energy barrier $\Delta g(r = r^*)$. Therefore, if we assume $\Delta G \propto \Delta T$, the thermodynamic term is proportional to $\exp(-\frac{1}{T(\Delta T)^2})$. On the other hand, the kinetic term is proportional to $\exp(-\frac{1}{T})$. As a result, the crystallization rate $I \propto \exp(-\frac{1}{T(\Delta T)^2}) \times \exp(-\frac{1}{T})$ exhibits a maximum at a nose temperature T_{nose} (see Fig. S4c).

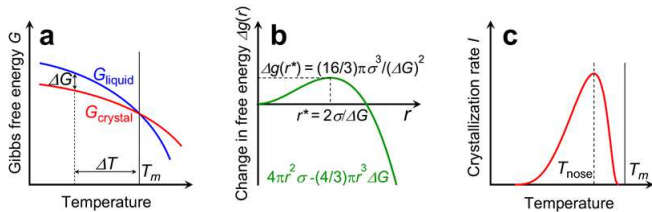


Fig. S4. (a) Gibbs free energies of the liquid and crystal phases. (b) Change in the total free energy caused by the nucleated crystalline phase, $\Delta g(r)$. At the critical radius $r^* = 2\sigma / \Delta G$, $\Delta g(r^*) = (16/3)\pi \sigma^3 / (\Delta G)^2$. (c) Crystallization rate derived from nucleation and growth theory. A characteristic peak structure appears at T_{nose} .

VII. COMPARISON WITH TIME-TEMPERATURE-TRANSFORMATION (TTT) AND CONTINUOUS HEATING TRANSFORMATION (CHT) DIAGRAMS

Figure S5a shows the relation between the resistivity of the sample, ρ_m , and the CO volume fraction, ϕ , derived from the GEM equation (see Sec. V). For the 2D triangular lattice, the critical volume fraction ϕ_0 at which the percolation path is closed by the insulating CO domains is estimated to be 0.66 [S25]. Indeed, $\rho_m(\phi)$ has an inflection point at ϕ_0 (see Fig. S5a). To check the validity of the GEM equation for the estimation of $\phi(t)$ from the resistivity, we reexamined the charge crystallization process in θ_m -TiZn by measuring the resistivity in the heating process with various sweeping rates after rapid cooling (Fig. S5b). This experimental procedure constructs a so-called continuous-heating-transformation (CHT) diagram. As shown in Fig. S5b, charge crystallization has been observed as an abrupt increase in resistivity. We defined the crystallization temperature T_X as the onset temperature of the abrupt increase (see Fig. S5b). The obtained T_X is plotted along with the TTT diagram in Fig. S5c, which shows that the critical volume fraction $\phi_0 \approx 0.66$ determined from the percolation theory coincides comparatively well with the value obtained from the CHT diagram. This result supports

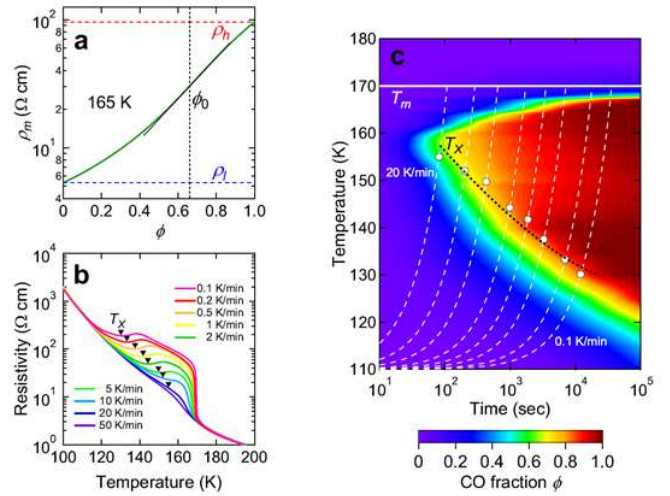


Fig. S5. (a) Log plot of ρ_m as a function of ϕ at 165 K. The black solid line represents the slope of $\rho_m(\phi)$ at the reflection point ϕ_0 . Here, $\rho_l \equiv 1/\sigma_h$ and $\rho_h \equiv 1/\sigma_l$ (see Sec. V for the definitions of σ_l and σ_h). (b) Temperature dependence of the resistivity measured in the heating process with various sweeping rates (0.1, 0.2, 0.5, 1, 2, 5, 10, 20, and 50 K/min) after rapid cooling. The inverted triangles indicate the crystallization temperature T_X for each sweeping rate. (c) TTT diagram along with the CHT diagram. The white dashed curves represent the time dependence of the temperature for each resistivity measurement starting from 110 K, at which $\rho(T)$ in (b) begins to show a clear sweeping-rate dependence. The sweeping rates are 0.1–20 K/min from right bottom to left top. The elapsed time in the heating process of the CHT diagram with a sweeping rate of R is defined as $t_R^{\text{CHT}}(T) = t_R(T) - t_{R=50 \text{ K/min}}(T)$. The block dotted curve is a guide for the eyes.

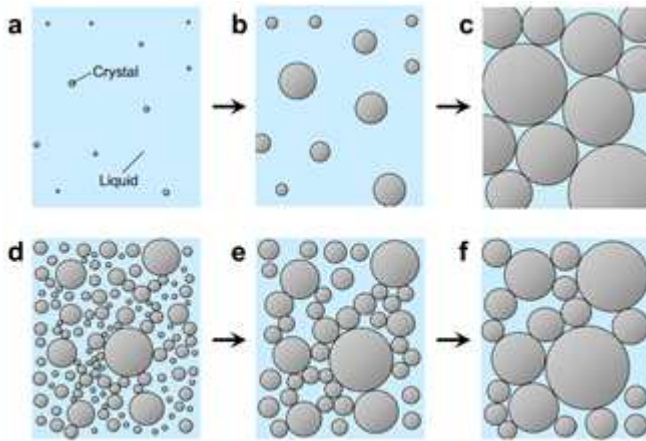


Fig. S6. (a)–(c) Schematic illustrations of the nucleation and growth process described by the JMAK formula. The gray circles stand for crystal domains with various radii, while the blue area represents the liquid region. Time evolves from (a) to (c). (d)–(f) Schematic illustrations of the Ostwald ripening process. Time evolves from (d) to (f). The smaller domains shrink, whereas the larger domains grow. The driving force comes from the difference in the total surface energy of the crystal-liquid interface among the domains, which arises from the difference in the radius of the domains. The system tends to minimize the interfacial free energy.

the validity of the GEM equation for the estimation of the CO volume fraction from the resistivity.

VIII. JOHNSON-MEHL-AVRAMI-KOLMOGOROV (JMAK) AND OSTWALD RIPENING PROCESSES

In a general nucleation and growth process, the crystallization rate at a constant temperature below T_m can be given by the Johnson-Mehl-Avrami-Kolmogorov (JMAK) equation, $\phi(t) = 1 - \exp(-kt^n)$, where k and n are the JMAK parameters [S27] (see Figs. 4d–f). The JMAK equation describes how the crystalline phase develops from the liquid phase. The initial slow crystallization rate can be attributed to the time to form a large number of nuclei of the crystalline phase (Fig. S6a). In the intermediate region, the crystallization rate strongly increases as the nuclei grow into particles (Fig. S6b). In the final stage of the nucleation and growth process, many boundaries are formed, where crystal growth stops (Fig. S6c). By contrast, Ostwald ripening is a crystallization process in which larger crystal domains further grow at the expense of smaller ones [S28] (Figs. S6d–f). In general, atoms or molecules on surfaces of a crystal are less stable than those of the interior, which causes a surface energy loss on the crystal-liquid interface. Therefore, domains with a large radius, in which the proportion of the interfacial surface energy relative to the total free energy is small, are energetically favored as compared to smaller domains. In other words, the system prefers a rearrangement of crystal grain boundaries through the Ostwald ripening process in order to minimize the total surface area. Thus, the small domains dissolve and adsorb onto the larger domains. The moderate time evolution of $\phi(t)$ observed in the final stage of crystal growth for θ_m -TlZn in the temperature range between the nose temperature and T_g can be well described by the Ostwald ripening process, $\phi(t) = 1 - (1 + k't)^{-1/3}$, where k' is a constant [S29] (see Fig. 4e).

-
- [S1] J. Müller, Fluctuation spectroscopy: A new approach for studying low-dimensional molecular metals. *ChemPhysChem* **12**, 1222–1245 (2011).
- [S2] H. Mori, S. Tanaka, T. Mori, A. Kobayashi, H. Kobayashi, Crystal structure and physical properties of M=Rb and Tl salts of (BEDT-TTF)₂MM'(SCN)₄ [M'=Co, Zn]. *Bull. Chem. Soc. Jpn* **71**, 797–806 (1998).
- [S3] T. Mori, Non-stripe charge order in the θ -phase organic conductors. *J. Phys. Soc. Jpn* **72**, 1469–1475 (2003).
- [S4] K. Suzuki, K. Yamamoto, K. Yakushi, Charge-ordering transition in orthorhombic and monoclinic single-crystals of θ -(BEDT-TTF)₂TlZn(SCN)₄ studied by vibrational spectroscopy. *Phys. Rev. B* **69**, 085114 (2004).
- [S5] H. Oike *et al.*, Phase-change memory function of correlated electrons in organic conductors. *Phys. Rev. B* **91**, 041101(R) (2015).
- [S6] R. T. Clay, S. Mazumdar, D. K. Campbell, Charge ordering in θ -(BEDT-TTF)₂X materials. *J. Phys. Soc. Jpn* **71**, 1816–1819 (2002).
- [S7] M. Kaneko, M. Ogata, Mean-field study of charge order with long periodicity in θ -(BEDT-TTF)₂X. *J. Phys. Soc. Jpn* **75**, 014710 (2006).
- [S8] H. Watanabe, M. Ogata, Novel charge order and superconductivity in two-dimensional frustrated lattice at quarter filling. *J. Phys. Soc. Jpn* **75**, 063702 (2006).
- [S9] K. Kuroki, The origin of the charge ordering and its relevance to superconductivity in θ -(BEDT-TTF)₂X: The effect of the Fermi surface nesting and the distant electron-electron interactions. *J. Phys. Soc. Jpn* **75**, 114716 (2006).
- [S10] M. Udagawa, Y. Motome, Charge ordering and coexistence of charge fluctuations in quasi-two-dimensional organic conductors θ -(BEDT-TTF)₂X. *Phys. Rev. Lett.* **98**, 206405 (2007).
- [S11] S. Nishimoto, M. Shingai, Y. Ohta, Coexistence of distinct charge fluctuations in θ -(BEDT-TTF)₂X. *Phys. Rev. B* **78**, 035113 (2008).
- [S12] M. Naka, H. Seo, Long-period charge correlations in charge-frustrated molecular θ -(BEDT-TTF)₂X. *J. Phys. Soc. Jpn* **83**, 053706 (2014).
- [S13] H. Wannier, Antiferromagnetism. The triangular Ising net. *Phys. Rev.* **79**, 357–364 (1950).
- [S14] R. M. F. Houtappel, Order-disorder in hexagonal lattices. *Physica* **16**, 425–455 (1950).
- [S15] C. Hotta, N. Furukawa, Strong coupling theory of the spinless charges on triangular lattices: Possible formation of a gapless charge-ordered liquid. *Phys. Rev. B* **74**, 193107 (2006).

- [S16] Y. Han *et al.*, Geometric frustration in buckled colloidal monolayers. *Nature* **456**, 898–903 (2008).
- [S17] M. Watanabe, Y. Noda, Y. Nogami, H. Mori, Investigation of X-ray diffuse scattering in θ -(BEDT-TTF)₂RbM'SCN₄. *Synth. Met.* **135–136**, 665–666 (2003).
- [S18] M. Watanabe, Y. Noda, Y. Nogami, H. Mori, Transfer integrals and the spatial pattern of charge ordering in θ -(BEDT-TTF)₂RbZn(SCN)₄ at 90 K. *J. Phys. Soc. Jpn* **73**, 116–122 (2004).
- [S19] F. Kagawa *et al.*, Charge-cluster glass in an organic conductor. *Nature Phys.* **9**, 419–422 (2013).
- [S20] M. Watanabe, Y. Nogami, K. Oshima, H. Mori, S. Tanaka, Novel pressure-induced $2k_F$ CDW state in organic low-dimensional compound θ -(BEDT-TTF)₂CsCo(SCN)₄. *J. Phys. Soc. Jpn* **68**, 2654–2663 (1999).
- [S21] Y. Nogami *et al.*, Structural modulation in θ -(BEDT-TTF)₂CsM'(SCN)₄ [M'=Co, Zn]. *Synth. Met.* **103**, 1911 (1999).
- [S22] T. Sato *et al.*, Emergence of nonequilibrium charge dynamics in a charge-cluster glass. *Phys. Rev. B* **89**, 121102(R) (2014).
- [S23] A. Painelli, A. Girlando, Electron-molecular vibration (e-mv) coupling in charge-transfer compounds and its consequences on the optical spectra: A theoretical framework. *J. Chem. Phys.* **84**, 5655–5671 (1986).
- [S24] D. S. McLachlan, M. Blaszkiewicz, R. E. Newnham, Electrical resistivity of composites. *J. Am. Ceram. Soc.* **73**, 2187–2203 (1990).
- [S25] V. A. Vyssotsky, S. B. Gordon, H. L. Frisch, J. M. Hammerley, Critical percolation probabilities (bond problem). *Phys. Rev.* **123**, 1566–1567 (1961).
- [S26] D. Stauffer, A. Aharony, *Introduction to Percolation Theory*. Taylor and Francis, London, second edition, (1994).
- [S27] M. Avrami, Kinetics of phase change. I General theory. *J. Chem. Phys.* **7**, 1103 (1939).
- [S28] J. H. Yao, K. R. Elder, H. Guo, M. Grant, Theory and simulation of Ostwald ripening. *Phys. Rev. B* **47**, 14110–14125 (1993).
- [S29] I. M. Lifshitz, V. V. Slyozov, The kinetics of precipitation from supersaturated solid solutions. *J. Phys. Chem. Solids.* **19**, 35–50 (1961).